Research Article | Vol. 7, No. 10 | 1 Oct 2016 | BIOMEDICAL OPTICS EXPRESS 4139

Biomedical Optics EXPRESS

Wide-field optical coherence micro-elastography for intraoperative assessment of human breast cancer margins

WES M. ALLEN,[1,2,*] LIXIN CHIN,[1,2] PHILIP WIJESINGHE,[1] RODNEY W. KIRK,[1,3] BRUCE LATHAM,[4] DAVID D. SAMPSON,[1,5] CHRISTOBEL M. SAUNDERS,[6,7,8] AND BRENDAN F. KENNEDY[1,2]

[1]*Optical + Biomedical Engineering Laboratory, School of Electrical, Electronic & Computer Engineering, The University of Western Australia, 35 Stirling Highway, Perth, WA 6009, Australia*
[2]*BRITElab, Harry Perkins Institute of Medical Research, QEII Medical Centre, 6 Verdun Street, Nedlands, WA 6009, Australia*
[3]*Centre for Nanoscale BioPhotonics, Faculty of Health Science, University of Adelaide, Adelaide, SA 5005, Australia*
[4]*PathWest, Fiona Stanley Hospital, 11 Robin Warren Drive, Murdoch, WA 6150, Australia*
[5]*Centre for Microscopy, Characterisation & Analysis, The University of Western Australia, 35 Stirling Highway, Perth, WA 6009, Australia*
[6]*School of Surgery, The University of Western Australia, 35 Stirling Highway, Perth, WA 6009, Australia*
[7]*Breast Centre, Fiona Stanley Hospital, 11 Robin Warren Drive, Murdoch, WA 6150, Australia*
[8]*Breast Clinic, Royal Perth Hospital, 197 Wellington Street, Perth, WA 6000, Australia*
**wes.allen@research.uwa.edu.au*

Abstract: Incomplete excision of malignant tissue is a major issue in breast-conserving surgery, with typically 20 - 30% of cases requiring a second surgical procedure arising from postoperative detection of an involved margin. We report advances in the development of a new intraoperative tool, optical coherence micro-elastography, for the assessment of tumor margins on the micro-scale. We demonstrate an important step by conducting whole specimen imaging in intraoperative time frames with a wide-field scanning system acquiring mosaicked elastograms with overall dimensions of ~50 × 50 mm, large enough to image an entire face of most lumpectomy specimens. This capability is enabled by a wide-aperture annular actuator with an internal diameter of 65 mm. We demonstrate feasibility by presenting elastograms recorded from freshly excised human breast tissue, including from a mastectomy, lumpectomies and a cavity shaving.

OCIS codes: (110.4500) Optical coherence tomography; (170.0170) Medical optics and biotechnology.

References and links

1. R. L. Siegel, K. D. Miller, and A. Jemal, "Cancer statistics, 2015," CA Cancer J. Clin. **65**(1), 5–29 (2015).
2. "Breast Cancer Facts & Figures 2015-2016" (American Cancer Society, 2015), retrieved http://www.cancer.org/acs/groups/content/@research/documents/document/acspc-046381.pdf.
3. C. C. Park, M. Mitsumori, A. Nixon, A. Recht, J. Connolly, R. Gelman, B. Silver, S. Hetelekidis, A. Abner, J. R. Harris, and S. J. Schnitt, "Outcome at 8 years after breast-conserving surgery and radiation therapy for invasive breast cancer: influence of margin status and systemic therapy on local recurrence," J. Clin. Oncol. **18**(8), 1668–1675 (2000).
4. S. E. Singletary, "Surgical margins in patients with early-stage breast cancer treated with breast conservation therapy," Am. J. Surg. **184**(5), 383–393 (2002).
5. H. Ballal, D. B. Taylor, A. G. Bourke, B. Latham, and C. M. Saunders, "Predictors of re-excision in wire-guided wide local excision for early breast cancer: a Western Australian multi-centre experience," ANZ J. Surg. **85**(7-8), 540–545 (2015).
6. R. Jeevan, D. A. Cromwell, M. Trivella, G. Lawrence, O. Kearins, J. Pereira, C. Sheppard, C. M. Caddy, and J. H. van der Meulen, "Reoperation rates after breast conserving surgery for breast cancer among women in England: retrospective study of hospital episode statistics," BMJ **345**(jul12 2), e4505 (2012).

#268575 http://dx.doi.org/10.1364/BOE.7.004139
Journal © 2016 Received 21 Jun 2016; revised 20 Aug 2016; accepted 24 Aug 2016; published 19 Sep 2016

Biomedical Optics EXPRESS

7. E. D. Kurniawan, M. H. Wong, I. Windle, A. Rose, A. Mou, M. Buchanan, J. P. Collins, J. A. Miller, R. L. Gruen, and G. B. Mann, "Predictors of surgical margin status in breast-conserving surgery within a breast screening program," Ann. Surg. Oncol. **15**(9), 2542–2549 (2008).
8. T. P. Olson, J. Harter, A. Muñoz, D. M. Mahvi, and T. Breslin, "Frozen section analysis for intraoperative margin assessment during breast-conserving surgery results in low rates of re-excision and local recurrence," Ann. Surg. Oncol. **14**(10), 2953–2960 (2007).
9. K. Esbona, Z. Li, and L. G. Wilke, "Intraoperative imprint cytology and frozen section pathology for margin assessment in breast conservation surgery: a systematic review," Ann. Surg. Oncol. **19**(10), 3236–3245 (2012).
10. R. A. Graham, M. J. Homer, C. J. Sigler, H. Safaii, C. H. Schmid, D. J. Marchant, and T. J. Smith, "The efficacy of specimen radiography in evaluating the surgical margins of impalpable breast carcinoma," AJR Am. J. Roentgenol. **162**(1), 33–36 (1994).
11. L. F. Smith, I. T. Rubio, R. Henry-Tillman, S. Korourian, and V. S. Klimberg, "Intraoperative ultrasound-guided breast biopsy," Am. J. Surg. **180**(6), 419–423 (2000).
12. N. Cabioglu, K. K. Hunt, A. A. Sahin, H. M. Kuerer, G. V. Babiera, S. E. Singletary, G. J. Whitman, M. I. Ross, F. C. Ames, B. W. Feig, T. A. Buchholz, and F. Meric-Bernstam, "Role for intraoperative margin assessment in patients undergoing breast-conserving surgery," Ann. Surg. Oncol. **14**(4), 1458–1471 (2007).
13. A. S. Haka, Z. Volynskaya, J. A. Gardecki, J. Nazemi, J. Lyons, D. Hicks, M. Fitzmaurice, R. R. Dasari, J. P. Crowe, and M. S. Feld, "In vivo margin assessment during partial mastectomy breast surgery using raman spectroscopy," Cancer Res. **66**(6), 3317–3322 (2006).
14. M. Jermyn, K. Mok, J. Mercier, J. Desroches, J. Pichette, K. Saint-Arnaud, L. Bernstein, M.-C. Guiot, K. Petrecca, and F. Leblond, "Intraoperative brain cancer detection with Raman spectroscopy in humans," Sci. Transl. Med. **7**(274), 274ra19 (2015).
15. F. T. Nguyen, A. M. Zysk, E. J. Chaney, J. G. Kotynek, U. J. Oliphant, F. J. Bellafiore, K. M. Rowland, P. A. Johnson, and S. A. Boppart, "Intraoperative evaluation of breast tumor margins with optical coherence tomography," Cancer Res. **69**(22), 8790–8796 (2009).
16. C. Zhou, D. W. Cohen, Y. Wang, H.-C. Lee, A. E. Mondelblatt, T.-H. Tsai, A. D. Aguirre, J. G. Fujimoto, and J. L. Connolly, "Integrated optical coherence tomography and microscopy for ex vivo multiscale evaluation of human breast tissues," Cancer Res. **70**(24), 10071–10079 (2010).
17. L. Scolaro, R. A. McLaughlin, B. F. Kennedy, C. M. Saunders, and D. D. Sampson, "A review of optical coherence tomography in breast cancer," Photonics Lasers Med. **3**(3), 225–240 (2014).
18. B. F. Kennedy, K. M. Kennedy, and D. D. Sampson, "A Review of Optical Coherence Elastography: Fundamentals, Techniques and Prospects," IEEE J. Sel. Top. Quantum Electron. **20**(2), 7101217 (2014).
19. B. F. Kennedy, K. M. Kennedy, A. L. Oldenburg, S. G. Adie, S. A. Boppart, and D. D. Sampson, *Optical Coherence Tomography: Technology and Applications* (Springer International Publishing, 2015), Chap. 32.
20. S. Wang and K. V. Larin, "Noncontact depth-resolved micro-scale optical coherence elastography of the cornea," Biomed. Opt. Express **5**(11), 3807–3821 (2014).
21. W. Qi, R. Chen, L. Chou, G. Liu, J. Zhang, Q. Zhou, and Z. Chen, "Phase-resolved acoustic radiation force optical coherence elastography," J. Biomed. Opt. **17**(11), 110505 (2012).
22. B. F. Kennedy, X. Liang, S. G. Adie, D. K. Gerstmann, B. C. Quirk, S. A. Boppart, and D. D. Sampson, "In vivo three-dimensional optical coherence elastography," Opt. Express **19**(7), 6623–6634 (2011).
23. B. F. Kennedy, R. A. McLaughlin, K. M. Kennedy, L. Chin, A. Curatolo, A. Tien, B. Latham, C. M. Saunders, and D. D. Sampson, "Optical coherence micro-elastography: mechanical-contrast imaging of tissue microstructure," Biomed. Opt. Express **5**(7), 2113–2124 (2014).
24. B. F. Kennedy, R. A. McLaughlin, K. M. Kennedy, L. Chin, P. Wijesinghe, A. Curatolo, A. Tien, M. Ronald, B. Latham, C. M. Saunders, and D. D. Sampson, "Investigation of optical coherence micro-elastography as a method to visualize cancers in human breast tissue," Cancer Res. **75**(16), 3236–3245 (2015).
25. A. C. Neuschatz, T. DiPetrillo, M. Steinhoff, H. Safaii, M. Yunes, M. Landa, M. Chung, B. Cady, and D. E. Wazer, "The value of breast lumpectomy margin assessment as a predictor of residual tumor burden in ductal carcinoma in situ of the breast," Cancer **94**(7), 1917–1924 (2002).
26. K. M. Kennedy, C. Ford, B. F. Kennedy, M. B. Bush, and D. D. Sampson, "Analysis of mechanical contrast in optical coherence elastography," J. Biomed. Opt. **18**(12), 121508 (2013).
27. A. B. Vakhtin, D. J. Kane, W. R. Wood, and K. A. Peterson, "Common-path interferometer for frequency-domain optical coherence tomography," Appl. Opt. **42**(34), 6953–6958 (2003).
28. B. F. Kennedy, S. H. Koh, R. A. McLaughlin, K. M. Kennedy, P. R. T. Munro, and D. D. Sampson, "Strain estimation in phase-sensitive optical coherence elastography," Biomed. Opt. Express **3**(8), 1865–1879 (2012).
29. L. Chin, A. Curatolo, B. F. Kennedy, B. J. Doyle, P. R. T. Munro, R. A. McLaughlin, and D. D. Sampson, "Analysis of image formation in optical coherence elastography using a multiphysics approach," Biomed. Opt. Express **5**(9), 2913–2930 (2014).
30. G. Lamouche, B. F. Kennedy, K. M. Kennedy, C.-E. Bisaillon, A. Curatolo, G. Campbell, V. Pazos, and D. D. Sampson, "Review of tissue simulating phantoms with controllable optical, mechanical and structural properties for use in optical coherence tomography," Biomed. Opt. Express **3**(6), 1381–1398 (2012).
31. R. A. McLaughlin, L. Scolaro, P. Robbins, S. Hamza, C. Saunders, and D. D. Sampson, "Imaging of human lymph nodes using optical coherence tomography: potential for staging cancer," Cancer Res. **70**(7), 2579–2584 (2010).

Biomedical Optics EXPRESS

32. M. Singh, C. Wu, C.-H. Liu, J. Li, A. Schill, A. Nair, and K. V. Larin, "Phase-sensitive optical coherence elastography at 1.5 million A-Lines per second," Opt. Lett. **40**(11), 2588–2591 (2015).
33. B. F. Kennedy, F. G. Malheiro, L. Chin, and D. D. Sampson, "Three-dimensional optical coherence elastography by phase-sensitive comparison of C-scans," J. Biomed. Opt. **19**(7), 076006 (2014).
34. V. Y. Zaitsev, A. L. Matveyev, L. A. Matveev, G. V. Gelikonov, E. V. Gubarkova, N. D. Gladkova, and A. Vitkin, "Hybrid method of strain estimation in optical coherence elastography using combined sub-wavelength phase measurements and supra-pixel displacement tracking," J. Biophotonics **9**(5), 499–509 (2016).
35. R. W. Kirk, B. F. Kennedy, D. D. Sampson, and R. A. McLaughlin, "Near video-rate optical coherence elastography by acceleration with a graphics processing unit," J. Lightwave Technol. **33**(16), 3481–3485 (2015).
36. A. A. Oberai, N. H. Gokhale, S. Goenezen, P. E. Barbone, T. J. Hall, A. M. Sommer, and J. Jiang, "Linear and nonlinear elasticity imaging of soft tissue in vivo: demonstration of feasibility," Phys. Med. Biol. **54**(5), 1191–1207 (2009).
37. T. A. Krouskop, T. M. Wheeler, F. Kallel, B. S. Garra, and T. Hall, "Elastic moduli of breast and prostate tissues under compression," Ultrason. Imaging **20**(4), 260–274 (1998).
38. K. M. Kennedy, L. Chin, R. A. McLaughlin, B. Latham, C. M. Saunders, D. D. Sampson, and B. F. Kennedy, "Quantitative micro-elastography: imaging of tissue elasticity using compression optical coherence elastography," Sci. Rep. **5**, 15538 (2015).
39. K. M. Kennedy, S. Es'haghian, L. Chin, R. A. McLaughlin, D. D. Sampson, and B. F. Kennedy, "Optical palpation: optical coherence tomography-based tactile imaging using a compliant sensor," Opt. Lett. **39**(10), 3014–3017 (2014).

1. Introduction

Breast cancer has the second highest mortality rate of cancers in females [1]. Surgical excision of malignant tissue forms a central component of breast cancer treatment [2]. The two most common surgical procedures are mastectomy and breast-conserving surgery (BCS). In the USA, for example, BCS accounts for ~58% of surgeries in patients diagnosed with early stage breast cancer [2].

In BCS, the surgeon's aim is to remove the entire tumor along with a rim of surrounding healthy tissue, referred to as the surgical margin, whilst ensuring a good cosmetic outcome for the patient. The current gold standard in assessing tumor margins is histopathological analysis, often performed days after surgery. If tumor is located at the cut edge of the removed tissue, it is classified as a positive margin. If tumor is found within a predetermined distance from the cut edge, it is classified as a close margin. This specified distance varies between institutions and is often between 0 and 5 mm [3, 4]. If no tumor is found on the cut edge or within the margin, it is classified as a negative margin. Currently, ~20 - 30% of patients undergo a re-excision procedure to remove additional tissue due to detection of an involved (positive or close) margin [5–7].

A major challenge for surgeons during BCS is the lack of effective tools to assess the surgical margin intraoperatively. Such tools would enable the surgeon to more effectively remove all tumor during the initial surgery, hence reducing re-excision rates. A range of intraoperative techniques are currently used, including: frozen section analysis [8], imprint cytology [9], intraoperative specimen radiography [10] and intraoperative ultrasound [11]. However, these techniques are time consuming and reported positive margin rates using these techniques are greater than 20% [12]. To address this issue, a number of new optical methods have been proposed for tumor margin assessment, including Raman spectroscopy [13, 14] and optical coherence tomography (OCT) [15, 16]. In particular, OCT holds great promise for margin assessment due to its high resolution (2-10 μm), rapid imaging speed and imaging depth of 1-2 mm [15, 17]. A challenge for OCT is that, whilst it readily differentiates adipose from dense tissue, it often lacks the contrast to differentiate tumor from uninvolved stroma [16].

Our group has been developing optical coherence elastography (OCE) to improve contrast in OCT by probing the mechanical properties of tissue. OCE utilizes OCT to measure tissue deformation induced by a mechanical load, and maps this information into an image (elastogram) of a mechanical property or parameter of the tissue [18]. Various OCE techniques have been developed with different loading and detection methods for various applications [19], including in ophthalmology [20], cardiology [21] and dermatology [22]. In

Biomedical Optics EXPRESS

our technique, termed optical coherence micro-elastography (OCME), a variant of compression, phase-sensitive OCE, a quasi-static deformation is introduced to the tissue between the acquisition of OCT B-scans [23]. We have recently published a feasibility study on 58 specimens demonstrating that compression OCME can provide enhanced contrast between malignant tumor and uninvolved stroma in freshly excised human breast tissue [23, 24]. These results are limited to fields-of-view of ~20 × 20 mm by the internal diameter of the piezoelectric ring actuator. As lumpectomies have typical dimensions of ~50 × 50 × 30 mm [25], the limited field-of-view has restricted the proportion of the tissue that can be scanned without relocating the sample or the actuator. Whilst it would be possible to move the sample relative to the imaging window, this would be time consuming, requiring successive preloading and unloading of the sample, and the movement would make it challenging to co-register images. To address this, we have implemented a wide-field piezoelectric ring actuator allowing ~50 × 50 mm OCT images and elastograms to be generated.

In this paper, we describe this new wide-field imaging system, and demonstrate its operation by presenting wide-field OCT images and elastograms of a tissue mimicking silicone phantom and various representative freshly excised human breast specimens. In addition, we present an example in which compression OCME detected an involved margin in a freshly excised lumpectomy specimen from BCS. Our results demonstrate the feasibility of scanning large areas of lumpectomies, which is an important step towards practical intraoperative margin assessment.

2. Methods

2.1 Imaging system

Our OCME system, based on a Fourier-domain OCT system, has been described in detail previously [23, 26]. Briefly, the OCT system comprises a superluminescent diode light source with a central wavelength of 835 nm and a bandwidth of 50 nm, and the axial (z) and lateral (x-y) resolutions have been measured to be 8 μm (in air) and 11 μm, respectively. The OCT system is configured in common-path mode [27], where the interface between the imaging window and the sample is used as the reference reflector.

The sensitivity of the system has been measured to be 102 dB for an exposure time of 36 μs [23]. The exposure time used in this study was 2 μs (to avoid saturation of the detector). A compressive load is applied to the sample using the wide-aperture piezoelectric ring actuator, which is rigidly affixed to the imaging window. The ring actuator imparts an axial displacement of up to 10 μm to the surface of the sample. A pair of OCT B-scans, one unloaded, and one loaded, is acquired at each lateral position, and the phase difference between each pair is used to calculate the axial displacement within the sample. 3D strain elastograms are then generated by calculating the local axial strain at each pixel, defined as the slope of axial displacement with respect to depth, here over an axial fitting range of 100 μm, setting the OCME system axial resolution [28]. The lateral resolution of the OCME system matches that of the OCT system, 11 μm. The displacement sensitivity of the system has been measured to be 2.2 nm for an OCT signal-to-noise ratio of 27 dB [29].

In order to ensure contact between the sample and the imaging window, a bulk preload is applied corresponding to a strain (change in thickness / initial thickness) of typically ~10 – 20%. To perform OCME, a much smaller strain is imparted using the ring actuator, typically corresponding to less than 0.1% [28]. The ring actuator is driven by a square-wave synchronized to the OCT acquisition such that subsequent OCT B-scans are acquired at different loading positions. B-scans are acquired at a rate of 50 Hz, and the ring actuator driving frequency is 25 Hz. The lateral scanning range of the OCME system is set by the x and y galvanometer mirror scanning system. Single OCT images and elastograms acquired using our system have dimensions 10 × 10 × 2 mm.

Biomedical Optics EXPRESS

For tissue testing in this study, each 10 mm B-scan comprises 1,000 A-scans. OCT C-scans comprise 1,000 B-scans. To enable spatial and temporal averaging of the detected phase signal, OCME C-scans comprise 10,000 B-scans, acquired in pairs, every 2 µm. Each B-scan pair corresponds to one loaded and one unloaded B-scan. Five B-scan pairs are averaged to generate the presented elastograms. This scan density results in acquisition times for OCT images and elastograms of 20 s and 200 s, respectively.

2.2 Wide-field system

Since the lateral scanning range is limited to a field-of-view of 10 × 10 mm by the galvanometer mirror system, in previous studies [23, 24], we manually moved the imaging window and sample relative to the scan head to allow for the acquisition of elastograms of ~20 × 20 mm. Further increases in the field-of-view are restricted by the 25 mm aperture of the ring actuator used in those studies. To move OCME towards being a practical tool for an intraoperative setting, we have implemented a new system based on a much wider-aperture ring actuator.

The ring actuator (Piezomechanik GmbH) has an internal diameter of 65 mm, allowing for a scanning range of ~50 × 50 mm, a stroke of 10 µm, thickness of 22 mm and resonant frequency of 40 kHz. The imaging window, rigidly affixed to the actuator, has a thickness of 4 mm and a diameter of 75 mm. To acquire wide-field images, automated *x*-*y* translation stages are used to reposition the sample and actuator relative to the optical beam, as indicated in Fig. 1. Each stage has a travel distance of 100 mm, maximum velocity of 30 mm s^{-1}, maximum acceleration of 30 mm s^{-2} and an accuracy of 2 µm. In-house software controls the stages during OCT/OCME acquisition. After each image is acquired, the stages move the sample in steps of 9.5 mm, allowing images to overlap by 0.5 mm. A grid of up to 5 × 5 images is acquired per sample to generate a wide-field image, with further detail given in Section 2.3.

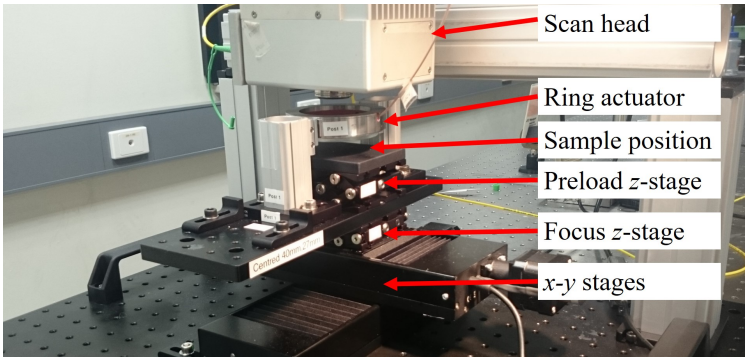

Fig. 1. Wide-field OCME system with main components labelled.

Due to the use of a common path configuration [27], it has previously been necessary to tilt the imaging window with respect to the beam axis in order to prevent saturation of the detector from strong back reflections. This tilt angle caused slight asymmetry in the coherence gate curvature but has negligible impact over a lateral scan range of 10 mm. Over a range of 50 mm, this tilt causes the focal plane to be sufficiently misaligned with the coherence plane to cause noticeable blurring in the wide-field *en face* image. To address this issue, adjustments were made to the tilt of the imaging window in the *x* and *y* axis to ensure it is flat relative to the optical table. In doing so, we ensure that the focal plane and coherence plane are aligned over the full range of the actuator. In order to prevent reflections from saturating the detector in this set up, we tilt the scan head ~2.5° relative to the imaging window. Due to the minor residual coherence gate curvature of the scanning system, small dark patches are present in the corners of each sub-image, as is particularly noticeable in the

Biomedical Optics EXPRESS

wide-field OCT image of the tissue mimicking phantom, Fig. 2(b). This artifact could be reduced by normalizing by the known effect of the curvature on the intensity; however, for this manuscript unaltered data are presented to allow the reader to fully interpret the experimental data acquired with this technique.

We firstly demonstrated wide-field OCME on a silicone tissue-mimicking phantom. Figure 2(a) shows a photograph of the phantom, which was fabricated using procedures similar to those described previously [30]. The phantom comprises stiff inclusions embedded in a soft matrix, with Young's moduli of 122 kPa and 6.4 kPa, respectively. The inclusions and matrix contain concentrations of 2.5 mg ml^{-1} and 0.8 mg ml^{-1} of optical scatterers (titanium dioxide), respectively. In total, 8 inclusions were incorporated into the phantom, embedded 300 µm below the surface of the matrix. The inclusions ranged in diameter from 0.5 mm to 21.4 mm and had a thickness of 1 mm. 25 elastograms were acquired to generate a wide-field elastogram of 47.5 × 47.5 mm. The white square in Fig. 2(a) corresponds to the imaged area. The wide-field *en face* OCT image, Fig. 2(b), taken at a depth of 400 µm, shows the inclusions embedded in the matrix. The wide-field *en face* elastogram, Fig. 2(c), exhibits increased contrast of the stiff inclusions to the soft matrix, particularly in the case of the smaller inclusions.

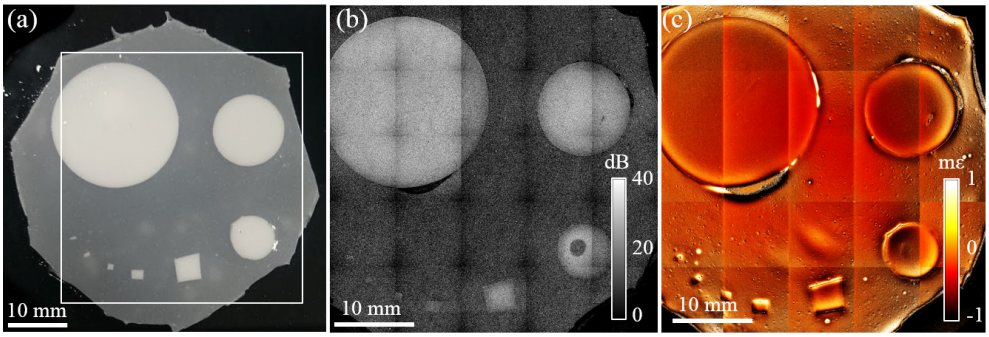

Fig. 2. Wide-field OCME of a tissue mimicking silicone phantom. (a) Photograph of phantom showing position of stiff inclusions. The white square indicates the area imaged using OCT and OCME. (b) Wide-field *en face* OCT image of phantom taken at a depth of 400 µm. (c) Wide-field *en face* elastogram of phantom taken at a depth of 400 µm.

2.3 Wide-field imaging protocol and processing

As described in Section 2.1, OCT images and elastograms acquired using our system have dimensions 10 × 10 × 2 mm. Wide-field *en face* OCT images and elastograms, of up to ~50 × 50 mm, are generated by acquiring a grid of these images and creating a wide-field mosaic. Existing tissue handling protocols at Fiona Stanley Hospital, Perth, Western Australia limit total scanning time for lumpectomies to ~30 min. Our acquisition protocol is designed to comply with this limit. Since single 10 × 10 × 2 mm elastograms take 200 s to acquire at a B-scan frequency of 50 Hz, it is not feasible to acquire 25 elastograms within the available time. In order to scan an entire face of the specimen, we have implemented the following procedure. Firstly, we acquire rapid 3D-OCT images; each acquired in ~20 s. *En face* OCT images are viewed live on in-house OCT acquisition software. OCME is then performed only in selected areas containing dense tissue. For a typical sample, we acquire 25 OCT images and 4 elastograms, resulting in a total acquisition time of ~30 min, including the time required to reposition the *x*-*y* stages.

OCT images and elastograms in this study are presented, as previously [24], in greyscale and linear false-colored colormaps, respectively. OCT shows excellent contrast between adipose, characterized by a distinct honeycomb structure [31], and dense tissue, characterized by high signal intensity, as shown in Fig. 3(a). As the main goal of OCME is to improve contrast in dense tissues, it is not necessary to perform OCME on adipose. In addition, as the

Biomedical Optics EXPRESS

OCT signal-to-noise ratio is low in adipose tissue, the accuracy of the detected phase is low, making it in any case challenging to perform OCME in these regions. In the results presented here, we present wide-field elastograms as OCT/OCME overlays, simply referred to as overlays, with strain presented only in areas of dense tissue.

Figure 3 shows the steps involved in generating and applying the masks. In this example, the image comprises a grid of 25 OCT images and 4 individual elastograms. In order to generate overlays, firstly the wide-field OCT image, Fig. 3(a), is cropped to remove all areas in which OCME has not been performed, Fig. 3(b). Thresholding is applied to the image in order to create a binary mask, Fig. 3(c). Upon visual inspection, additional filtering or manual erasing may be performed to remove residual areas of adipose not removed by the thresholding technique. The wide-field elastogram, Fig. 3(d), is then multiplied by the mask in order to remove strain information from regions of adipose, Fig. 3(e). In the final step, the masked elastogram is overlaid on the original wide-field OCT image to create the wide-field overlay shown in Fig. 3(f). All *en face* images of tissue presented in this study are taken at a depth of 100 µm from the imaging window. In the elastograms presented, the scale is millistrain ($\times 10^{-3}$ strain), mε, with negative corresponding to compression and positive strain corresponding to either tension or compression acting in the opposite direction to the applied force.

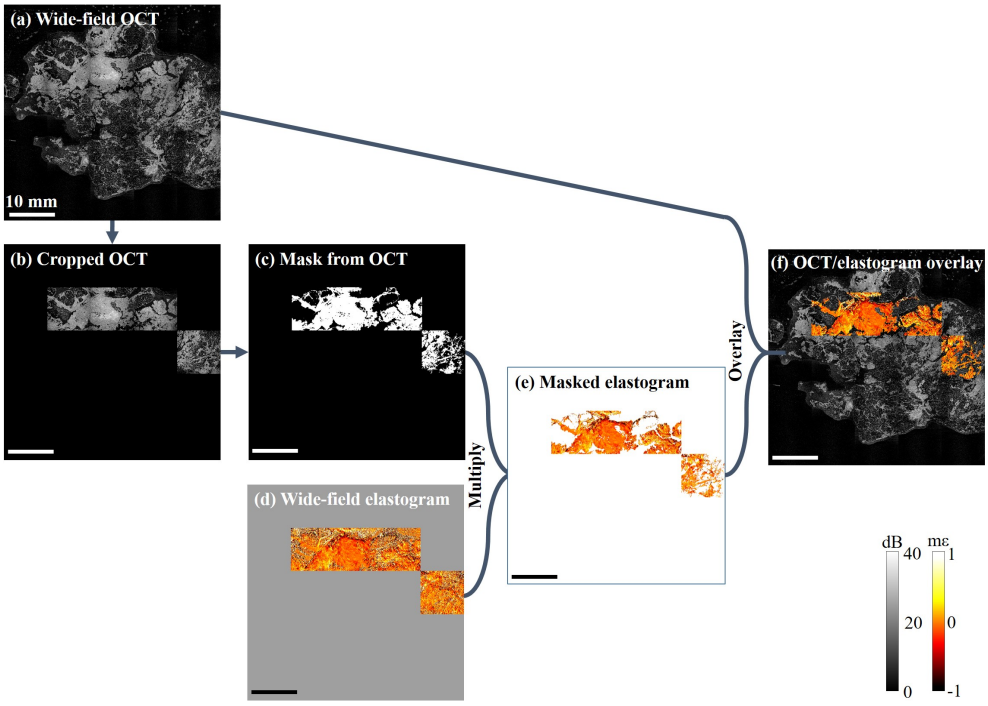

Fig. 3. Illustration of the overlay process. (a) Wide-field OCT image. (b) Cropped OCT image, generated by combining (a) and (d). (c) Binary mask. (d) Unmodified wide-field elastogram. (e) Masked elastogram, generated by multiplying (c) and (d), (white area corresponds to transparent in the overlay). (f) Wide-field OCT/OCME, generated by overlaying (e) onto (a). Scale bar 10 mm.

2.4 Tissue preparation

Informed consent was obtained from patients and the study approved by Fiona Stanley Hospital. Thirteen specimens were imaged, freshly excised from eight patients undergoing BCS, mastectomy or mastectomy with axillary clearance. After excision, lumpectomy specimens were imaged as received within ~30 min. Mastectomy samples were dissected to

Biomedical Optics EXPRESS

similar dimensions of a typical lumpectomy. Samples were placed on the *z*-axis translation stage (see Fig. 1), a bulk preload was applied, and we allowed a one minute delay to reduce to a negligible level the impact of viscoelastic creep on our images [28].

After imaging, samples were fixed in 10% neutral-buffered formalin, embedded in paraffin, sectioned, and stained with hematoxylin and eosin following the standard histopathology protocols used at Fiona Stanley Hospital. Histology images from the mastectomy specimen presented in Fig. 5 are in the same plane as the *en face* images. Histology images from the BCS specimens are in the plane orthogonal to the *en face* images, as seen in Fig. 6.

3. Results

Figures 4–7 contain wide-field OCT images and elastograms of four human breast tissue samples, freshly excised from three patients undergoing either a mastectomy procedure or BCS. In Fig. 4, we present images of a benign tumor excised from a 65-year-old patient undergoing a hookwire local excision. This wide-field *en face* overlay image, Fig. 4(a), measuring 38 × 38 mm, comprises 16 OCT images and 4 elastograms. In Fig. 4(a), large areas of dense tissue surrounded by adipose can be observed. A benign intraductal papilloma (P) is visible, as well as small regions of adipose (A) and uninvolved stroma (S), in the wide-field *en face* overlay. A photograph of the tissue is shown in Fig. 4(b). Figures 4(c) and 4(d) show a 1.6 × magnification of the OCT and overlay images, respectively. In both the OCT and overlay images, the papilloma appears to have a highly fibrous structure. The orientation of the fibers and the strain pattern appear to be more organized than we would expect from examples of malignant tumors from previous studies [24]. This suggests that, using OCT and OCME, we may be able to distinguish papillomas from malignant tissue.

In Fig. 5, we present images acquired from a dissected tumor, excised from a 34-year old patient undergoing a mastectomy procedure. The sample, measuring ~35 × 25 mm, contains high-grade tumor surrounded by adipose. The wide-field *en face* overlay image, Fig. 5(a), comprises 25 OCT images and 3 elastograms. OCT clearly delineates adipose (A), with areas of dense tissue (D) characterized by high signal-to-noise ratio. The histology image, Fig. 5(b), shows dense regions of tumor (T) interspersed with uninvolved stroma (S) and adipose tissue (A). Due to the size of the specimen, the tumor was dissected and loaded into four cassettes for histopathological analysis. For presentation in this paper, histology images from the cassettes have been manually stitched together. The horizontal white line visible in Fig. 5(b) is a result of this stitching process (C). We can see on the 1.6 × magnified OCT image, Fig. 5(c), there is limited contrast within the dense tissue. In the overlay of the same region, Fig. 5(d), we see a heterogeneous strain pattern indicative of tumor (T) and small areas with a homogeneous strain pattern, indicative of uninvolved stroma (S). Mechanical heterogeneity visible in malignant tumor is a result of differences in the mechanical properties and structure expected between the nests of tumor cells and the surrounding immature desmoplastic stroma, as described in detail in previous work [24]. The artifact in the center of Fig. 5(a) and bottom right of Figs. 5(c) and 5(d) is caused by there being no contact (NC) between the tissue and window. The heterogeneous strain pattern we see in areas of tumor is consistent with findings in our previous studies [23, 24].

Biomedical Optics EXPRESS

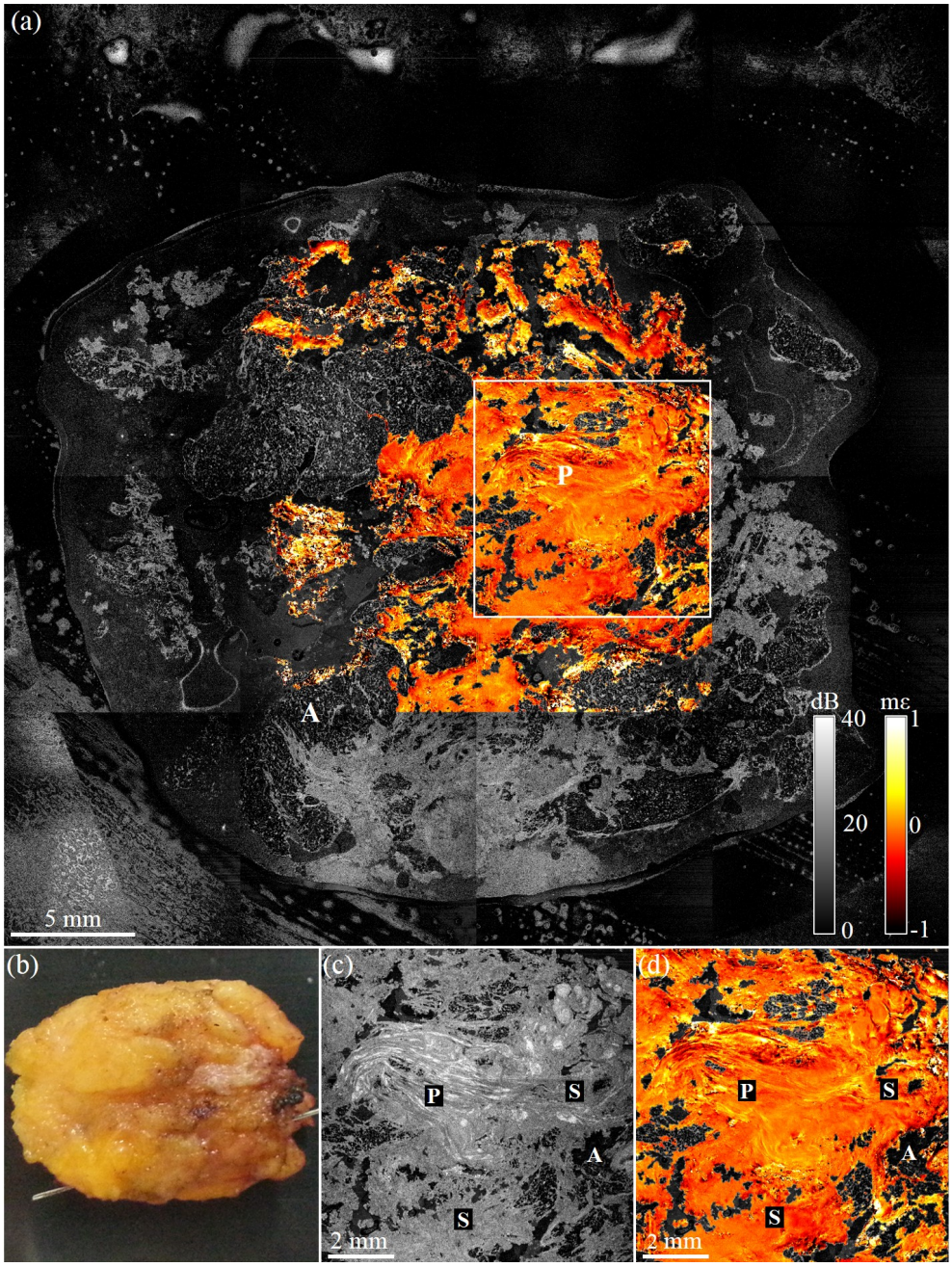

Fig. 4. Wide-field OCME of a freshly excised benign tumor. (a) Wide-field *en face* OCME overlay on OCT of benign tumor (b) Photograph of excised tissue. (c) *En face* OCT image showing a 1.6 × magnification of the boxed region in (a). (d) Corresponding *en face* OCME overlay. A, adipose; S, stroma; and P, intraductal papilloma.

Biomedical Optics EXPRESS

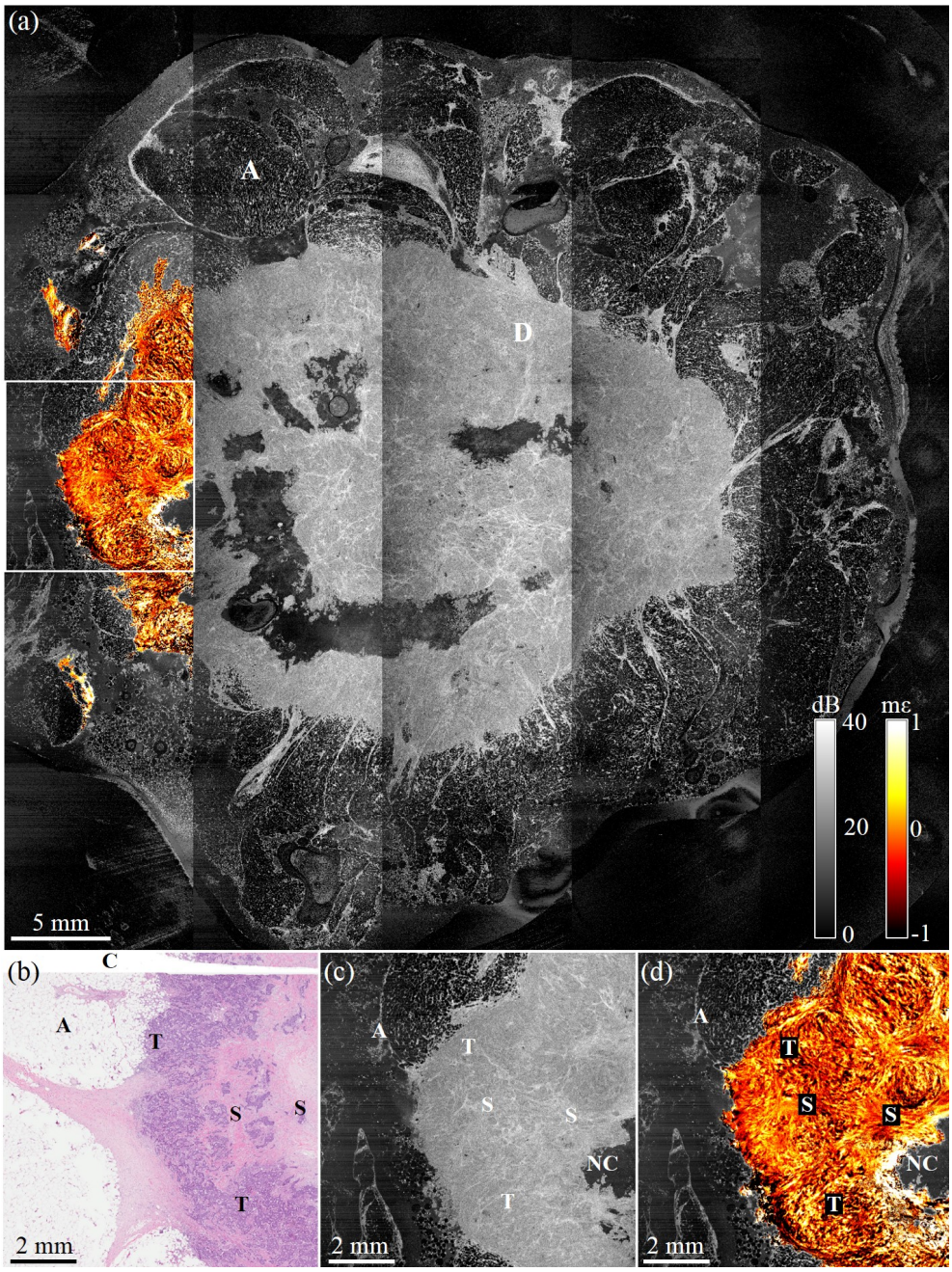

Fig. 5. Wide-field OCME of a freshly excised malignant tumor. (a) Wide-field *en face* OCME overlay on OCT of the entire sample, measuring 47.5 × 47.5 mm. (b) Histology, co-registered with OCT and OCME image. (The white horizontal artifact at top is due to stitching images taken from tissue in two histology cassettes.) (c) *En face* OCT image showing a 1.6 × magnification of the boxed region in (a). (d) Corresponding *en face* OCME overlay. A, adipose; C, cassette stitching artifact; D, dense tissue; NC, non-contact; S, stroma; and T, tumor.

In Fig. 6, we present images acquired from a lumpectomy, excised from a 46-year-old patient undergoing BCS. The wide-field *en face* overlay, Fig. 6(a), comprises 25 OCT images and 4 elastograms. Regions of dense tissue interspersed with adipose can be observed in Fig.

Biomedical Optics EXPRESS

6(a). Areas indicated by green and red squares are magnified by 1.6 × in Figs. 6(c), 6(d) and 6(f) and 6(g), respectively. Comparing the corresponding OCT images, Figs. 6(c) and 6(f), it is difficult to identify differences in structure between the two regions of dense tissue. However, in the overlay image, these two regions are easily distinguished by differing textures in the elastograms. The overlay, Fig. 6(d), shows uniform strain texture and is indicative of uninvolved stroma. In comparison, Fig. 6(g) shows a heterogeneous strain texture indicative of malignant tumor. These patterns in uninvolved and malignant tissue are consistent with our previous studies in breast tissue [24] and are confirmed by histology images acquired from the same region. The green and red dashed lines in Fig. 6(a) indicate the regions from which histology images are presented in Figs. 6(b) and 6(d), respectively. Following protocols used at Fiona Stanley Hospital for margin assessment, the histology images shown here, in contrast to that shown in Fig. 4, are taken orthogonal to the *en face* images, and the blue arrows indicate the direction of the imaging beam. Figure 6(b) does not contain malignant tissue; however, in Fig. 6(e), we see that this section of the lumpectomy has an involved margin. From visual inspection and manual palpation performed during the surgery, the surgeon suspected malignant tumor close to the surface of the excised lump and proceeded to excise additional tissue (cavity shaving). The cavity shaving, measuring ~17 × 23 mm, was taken from the wall of the cavity of the remaining breast tissue.

Figure 7 shows images acquired from the cavity shaving associated with the lumpectomy specimen shown in Fig. 6. The surface imaged corresponds to the new surgical margin. The wide-field *en face* overlay, Fig. 7(a), consists of 4 OCT images and 4 elastograms. The shaving comprises mostly adipose with small areas of dense tissue. Figures 7(a) and 7(d) show homogeneous strain texture, indicative of uninvolved stroma. Vertical striations present in elastograms presented in Fig. 7 are a ringing artifact seen in thin samples. Ringing occurs due to the ring actuator being driven by a step function and overshooting its set position, with this damped oscillation decaying over several A-scans in each B-scan. Histopathological analysis confirmed that this cavity shaving had a negative margin.

Biomedical Optics EXPRESS

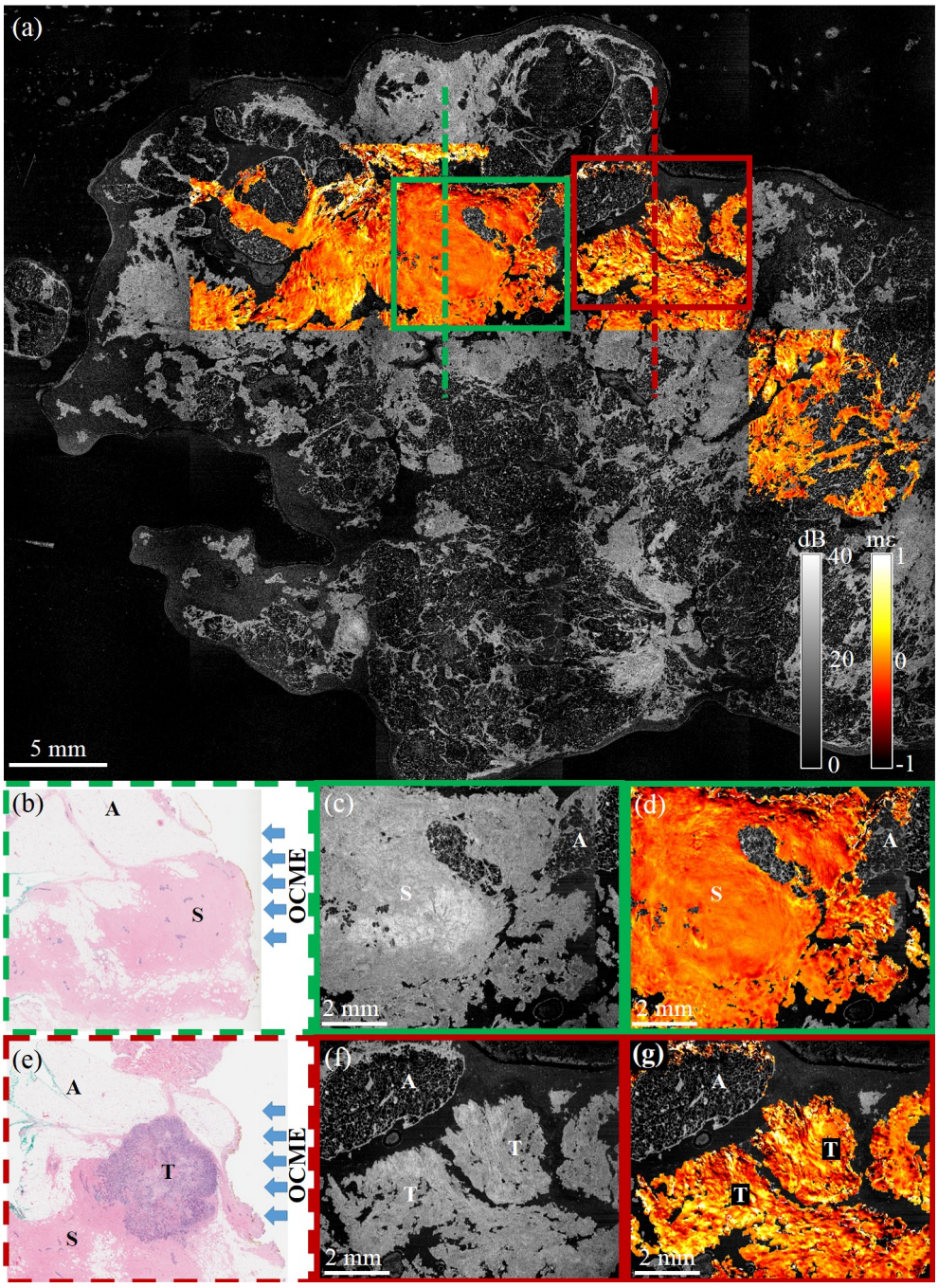

Fig. 6. Wide-field OCME of a freshly excised lumpectomy. (a) Wide-field *en face* OCME overlay on OCT of lumpectomy. (b) Histology acquired in orthogonal plane to OCT/OCME from region indicated by green dashed line found to contain clear margin. (c) *En face* OCT image showing a 1.6 × magnification of the green boxed region in (a). (d) Corresponding *en face* overlay. (e) Histology acquired in orthogonal plane to OCT/OCME from region indicated by red dashed line found to contain involved margin. (f) *En face* OCT image showing a 1.6 × magnification of the blue boxed region. (g) Corresponding *en face* overlay. Note: Histology is taken in the plane orthogonal to *en face* images, with the imaging beam direction indicated by blue arrows. A, adipose; S, stroma; and T, tumor.

Biomedical Optics EXPRESS

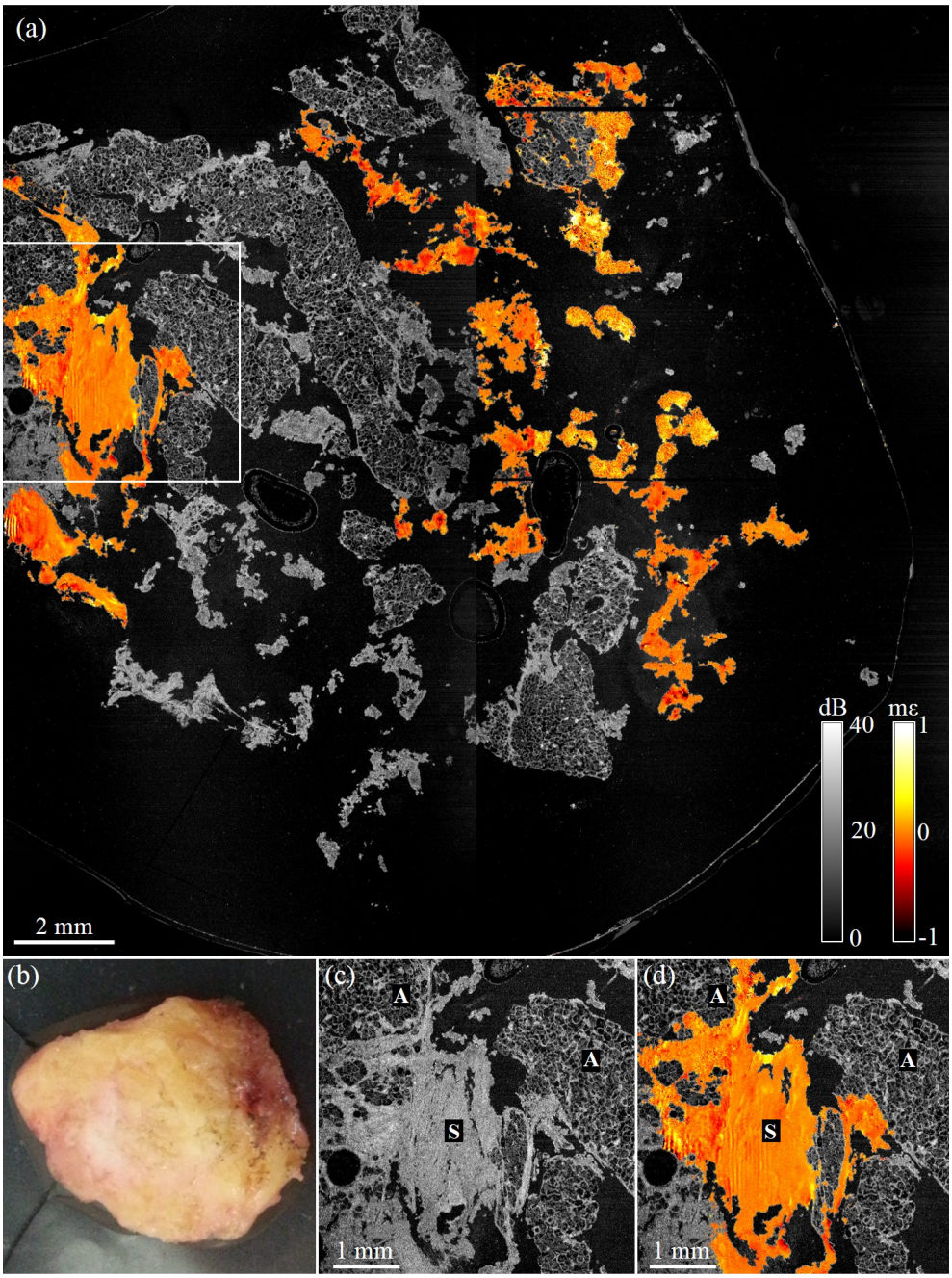

Fig. 7. Wide-field OCME of a freshly excised cavity shaving. (a) Wide-field *en face* OCME overlay on OCT of cavity shaving, black regions correspond to areas of noncontact or absence of tissue. (b) Photograph of sample. (c) *En face* OCT image showing a 1.6 × magnification of boxed region in (a). (d) Corresponding *en face* OCME overlay. A, adipose; and S, stroma.

4. Discussion

In this study, we have presented the first demonstration of wide-field compression OCME capable of assessing large areas of an excised lumpectomy specimen in an intraoperative timeframe and successfully detecting an involved margin. In the current configuration, this

Biomedical Optics EXPRESS

system is limited to scanning excised tissue. However, by permitting assessment of tumor margins in an intraoperative time frame, this study is an important step towards our objective of reducing the re-excision rate of patients undergoing breast-conserving surgery.

The total scanning time for freshly excised human tissue for this study is 30 min, ensuring that our imaging complied with existing tissue handling protocols at Fiona Stanley Hospital. We are currently developing methods to further reduce the time required to acquire and visualize data. One way in which the acquisition time could be reduced is by increasing the A-scan acquisition rate. In this current study, A-scans were acquired at a frequency of 50 kHz. Recent related OCE work has demonstrated a phase-sensitive technique with an A-scan frequency of 1.5 MHz, utilizing a Fourier-domain mode-locked (FDML) swept-source laser [32]. Implementing a similar FDML laser in compression OCME could increase acquisition speeds by a factor of 30. This could lead to 3D-OCT images being acquired in less than 1 s and 3D elastograms being acquired in ~7 s without a reduction in spatial or temporal averaging.

Increasing the A-scan frequency with an FDML laser, if implemented in the future, would require an increase of actuation frequency. An increased actuator frequency is likely to cause a ringing artifact, similar to that seen in Fig. 7(d), to occur more often [33]. Our group has previously published an acquisition method for compression OCME that could be implemented to overcome this ringing artifact by calculating the voxel-to-voxel phase difference between C-scans, compared to the technique used in this study in which we calculate the phase difference between B-scans. This method would allow us to increase the A-scan frequency through an FDML laser while avoiding the ringing artifact associated with a high actuator frequency.

An alternative method to reduce the acquisition time of 3D-OCME is to reduce the spatial averaging. Recent publications describe a method enabling this in which a larger strain results between subsequent B-scans [34]. The greater phase differences are less masked by measurement noise. Implementing a variation of this technique has the potential to reduce our acquisition time by a factor of 5, which may remove the need to incorporate expensive FDML lasers in our setup.

As well as reducing acquisition time, data processing time can also be reduced. Wide-field results, comprising 25 OCT and 4 OCME individual data sets, presented in this study took approximately 6 hours to process. In recent work, our group has demonstrated near video-rate OCME processing [35]. Utilizing a commercial-grade graphics processing unit and a desktop computer, the system achieved a processing rate of 21 B-scan elastograms per second. The masking and overlaying process described in Section 2.3 could also be automated using thresholding of the OCT image. Additional filtering would need to be incorporated to remove residual areas of adipose not removed by the thresholding technique, as described above. Incorporating this technique into our current system could enable elastograms to be presented and interpreted intraoperatively. A further step for this thresholding process is to use the binary mask generated to automatically select regions from which to capture OCME data.

Histology images in this study are presented in two different planes. In the case of the mastectomy specimen, as tissue was not required by the hospital for subsequent analysis, histology images were obtained in the same plane as wide-field *en face* images. In the case of the lumpectomy specimen, tissue was required for subsequent analysis, thus, in following the standard histopathology protocols used at Fiona Stanley Hospital, histology images could not be obtained in the same plane as our wide-field *en face* images.

In order for the ring actuator to impart a displacement to the sample, the sample must be in contact with the imaging window. This is currently achieved by applying a preload to the sample. This preload is typically in the region of ~10% of the thickest part of the sample. In some cases, it may be up to ~20%, depending on the geometry of the tissue. Due to the nonlinear properties of biological tissue, some features are more clearly delineated with

Biomedical Optics EXPRESS

micro-elastography when performed at higher preloads [36, 37]. However, in some cases, a preload of ~20% does not result in complete contact between the tissue and the imaging window. This can lead to artifact in regions of non-contact, as shown in Fig. 5(a). Another issue with non-contact is that it can lead to the generation of axial tensile strain associated with surface topography rather than with tissue properties. In future studies, we will investigate incorporating optical palpation to reduce artifacts generated by non-contact [38, 39]. In optical palpation, a thin, compliant and transparent layer is placed between the sample and the imaging window. The stiffness of the layer is designed to be similar to the stiffness of breast tissue. As preload is applied to the sample, the compliant layer deforms to partially fill areas of non-contact. Implementing a compliant layer in our wide-field system would allow more uniform contact without the need to preload the sample excessively. This technique would also allow us to quantify the tissue stiffness [38].

5. Conclusion

In conclusion, we have demonstrated that wide-field compression OCME can generate OCT images and elastograms of freshly excised human breast tissue over a field-of-view of up to ~50 × 50 mm. By rapidly acquiring OCT images and performing OCME in selected regions of dense tissue within 30 min, we have demonstrated the potential of wide-field OCME as a tool to intraoperatively assess surgical margins of excised breast tissue. We have presented an example which demonstrates that wide-field compression OCME can delineate malignant tissue and uninvolved stroma in a freshly excised lumpectomy sample. In this study, we have advanced OCME to the point of scanning lumpectomy specimens. In future work, we will incorporate further reductions in acquisition and processing time and determine the diagnostic accuracy of compression OCME in identifying malignant tissue during breast-conserving surgery.

Funding

This research was supported, in part, by grants and fellowships from the Australian Research Council, the National Health and Medical Research Council (Australia), the National Breast Cancer Foundation (Australia), the Department of Health, Western Australia, and a scholarship from the William and Marlene Schrader Trust of The University of Western Australia.